



HAL
open science

Harnessing subcellular-resolved organ distribution of cationic copolymer-functionalized fluorescent nanodiamonds for optimal delivery of therapeutic siRNA to a xenografted tumor in mice

Sandra Claveau, Marek Kindermann, Alexandre Papine, Zamira V Díaz-Riascos, Xavier Delen, Patrick Georges, Roser López-Alemaný, Òscar Tirado Martínez, Jean-Rémi Bertrand, Ibane Abasolo Olaortua, et al.

► To cite this version:

Sandra Claveau, Marek Kindermann, Alexandre Papine, Zamira V Díaz-Riascos, Xavier Delen, et al.. Harnessing subcellular-resolved organ distribution of cationic copolymer-functionalized fluorescent nanodiamonds for optimal delivery of therapeutic siRNA to a xenografted tumor in mice. 2021. hal-03085752v1

HAL Id: hal-03085752

<https://hal.science/hal-03085752v1>

Preprint submitted on 6 Jan 2021 (v1), last revised 27 May 2021 (v2)

HAL is a multi-disciplinary open access archive for the deposit and dissemination of scientific research documents, whether they are published or not. The documents may come from teaching and research institutions in France or abroad, or from public or private research centers.

L'archive ouverte pluridisciplinaire **HAL**, est destinée au dépôt et à la diffusion de documents scientifiques de niveau recherche, publiés ou non, émanant des établissements d'enseignement et de recherche français ou étrangers, des laboratoires publics ou privés.

Harnessing subcellular-resolved organ distribution of cationic copolymer-functionalized fluorescent nanodiamonds for optimal delivery of therapeutic siRNA to a xenografted tumor in mice

*Sandra Claveau[†], Marek Kindermann[†], Alexandre Papine[†], Zamira V. Díaz-Riascos, Xavier Délen, Patrick Georges, Roser López-Alemaný, Òscar Tirado Martínez, Jean-Rémi Bertrand, Ibane Abasolo, Petr Cigler, and François Treussart**

Dr S. Claveau, Prof. F. Treussart
Université Paris-Saclay, ENS Paris-Saclay, CNRS, CentraleSupélec, LuMIn, 91190 Gif-sur-Yvette, France
E-mail: francois.treussart@ens-paris-saclay.fr

Dr S. Claveau, Dr J.-R. Bertrand
Université Paris-Saclay, Institut Gustave Roussy, CNRS, Metabolic and Systemic Aspects of Oncogenesis (METSÝ), 94805 Villejuif, France.

M. Kindermann and Dr P. Cigler
Institute of Organic Chemistry and Biochemistry of the Czech Academy of Sciences, 166 10 Prague, Czech Republic

M. Kindermann
Department of Chemical Engineering, University of Chemistry and Technology, 166 28 Prague, Czech Republic

A. Papine
IMSTAR S.A., 75014 Paris, France

Dr Z. V. Díaz-Riascos, Dr I. Abasolo
Drug Delivery & Targeting, Functional Validation & Preclinical Research (FVPR), CIBBIM-Nanomedicine, Vall d'Hebron Institut de Recerca (VHIR), Universitat Autònoma de Barcelona (UAB), 08035 Barcelona, Spain

Dr Z. V. Díaz-Riascos, Dr I. Abasolo
Networking Research Center on Bioengineering, Biomaterials and Nanomedicine (CIBER-BBN), 08035 Barcelona, Spain

Dr X. Délen, Dr P. Georges
Université Paris-Saclay, Institut d'Optique Graduate School, CNRS, Laboratoire Charles Fabry, 91127 Palaiseau, France

Dr R. López-Alemaný, Dr Ò. Tirado Martínez
Sarcoma Research Group, Oncobell Program, Bellvitge Biomedical Research Institute (IDIBELL), 08908 L'Hospitalet de Llobregat, Barcelona, Spain

[†]These authors contributed equally to this work.

Keywords: *in vivo* siRNA delivery, fluorescent nanodiamond, cationic copolymer, biodistribution, time-delayed epifluorescence, high-throughput quantifications

Diamond nanoparticles (nanodiamonds) can transport active drugs in cultured cells as well as *in vivo*. However, in the latter case, methods allowing to determine their bioavailability accurately are still lacking. Nanodiamond can be made fluorescent with a perfectly stable emission and a lifetime ten times longer than the one of tissue autofluorescence. Taking advantage of these properties, we present an automated quantification method of fluorescent nanodiamonds (FND) in histological sections of mouse organs and tumor, after systemic injection. We use a home-made time-delayed fluorescence microscope comprising a custom pulsed laser source synchronized on the master clock of a gated intensified array detector. This setup allows to obtain ultra-high-resolution images 120 Mpixels of whole mouse organs sections, with subcellular resolution and single-particle sensitivity. As a proof-of-principle experiment, we quantified the biodistribution and aggregation state of new cationic FNDs able to transport small interfering RNA inhibiting the oncogene responsible for Ewing sarcoma. Image analysis showed a low yield of nanodiamonds in the tumor after intravenous injection. Thus, for the *in vivo* efficacy assay we injected the nanomedicine into the tumor. We achieved a 28-fold inhibition of the oncogene. This method can readily be applied to other nanoemitters with ≈ 100 ns lifetime.

1. Introduction

The *in vivo* efficacy of drugs is largely dependent on their bio-availability and -distribution after body administration. One strategy to optimize the tissue distribution relies on delivering the drugs with nanoparticles. It led to the emergence of the field of nanomedicine about 40 years ago. The quantitative assessment of nanomedicine distribution *in vivo* is most often done with apparatus dedicated to whole animal body imaging of radioelement, bioluminescence or fluorescence reporters (especially in the near infrared wavelength tissue transparency region) [1]. To date, the spatial resolution achieved by these apparatus does not allow to resolve single cell, reaching at best 20 μm (with the fluorescence molecular tomograph IVIS Spectrum, PerkinElmer, USA). Such low resolution makes the identification of the delivery and elimination pathways difficult, and motivates the development of cellular and sub-cellular resolved methods. The latter requires larger magnification and can be carried out either *in vivo* by intravital microscopy [2] and endoscopy [3], or *ex vivo* on tissue sections. In order to achieve a reliable quantification of the nanomedicine organ distribution at subcellular resolution, a large number of fields of views (FOV, typically of 100 μm in size) need to be recorded and analyzed, to cover a whole section, requiring an automatization of the process. Moreover, for its efficient detection the nanomedicine should possess a sufficiently large contrast and specificity in the imaging modality used. While advanced technologies as time-of-flight secondary ion mass spectroscopy imaging offer unique specificity along with sub-micrometer resolution [4], they are usually not carried out on whole organ section, as it can be more easily done by optical microscopy. In this domain, hyperspectral dark-field microscopy [5] has shown its ability to detect strongly scattering nanoparticles (*e.g.* gold nanoparticles) in *ex vivo* tissue section at the single particle level with subcellular resolution, allowing precise quantification of their biodistribution [6]. While it is a powerful method when dealing with strongly scattering material, it may be less efficient with other nanovector materials.

Among them, diamond nanocrystal (nanodiamond, size 5-50 nm) has been shown to be an efficient delivery agent of macromolecules such as anticancer compounds or siRNA into cells in culture or small organisms, and that can be traced by various remarkable modalities on unlimited timescale thanks to its perfectly stable structure [7–9]. The first modality is associated to the Raman scattering signature of diamond that was used in particular to evaluate the overall tissue distribution after whole organ digestion [10]. The second modality, which has popularized nanodiamonds these past fifteen years, is the possibility to entitle them with a perfectly photostable fluorescence by generating nitrogen-vacancy (NV) defects center within the diamond lattice, creating fluorescent nanodiamonds (FND) [8]. Upon green laser excitation, NV center emits in the 600-750 nm wavelength range and possess at least two additional unique properties of interest for tissue distribution. First of all, the negatively charged NV⁻ has an optically detectable electron spin resonance that is largely harnessed for sensitive magnetometry and quantum sensing [11], and was also used to implement a magnetic resonance imaging scheme and identify FND in tissue [12], but at a spatial resolution limited to 100 μ m. Secondly, the insertion of the NV center in the subwavelength scale sized nanodiamond lattice, results in an increase in its emission lifetime (\approx 20-40 ns) compared to bulk diamond environment (\approx 11 ns), due to a smaller local density of electromagnetic states [13]. FND emission lifetime is therefore about one order of magnitude longer than the one of tissue autofluorescence (\approx 3 ns [14]), allowing an efficient filtering of FND by time-gated detection in a sub-nanosecond pulsed excitation scheme [15]. This strategy was already exploited to monitor tissue regeneration by tracking FND-labelled stem cells in mouse lung section with single FND resolution [16], but it was not extended yet to their quantitative biodistribution.

Here we report the development of an automated imaging and analysis biodistribution pipeline able to (i) quantify the FND content in histological sections of mouse main organs after systemic injection, and to (ii) infer the cellular type thanks to histological staining, subcellular resolution and single particle resolution. We apply this method to the determination of the

optimal delivery route by nanodiamond of an anticancer compound to a tumor xenografted on mice. In the continuity of our previous work on the treatment of Ewing sarcoma (ES) [17,18] – a cancer in which cell proliferation is driven by the expression of a junction oncogene – we use a small interfering RNA (siRNA) to inhibit the oncogene. We also improve the siRNA electrostatic binding to FND using a linear cationic copolymer covalently grafted from the FND surface (Cop⁺-FND). This conjugate enables to protect siRNA against degradation in physiological environment and to deliver it efficiently to the cells. We validate the *in vitro* efficacy of the new Cop⁺-FND:siRNA to inhibit the oncogene in ES cell in culture, with an efficacy larger than the one reached previously with FND complexed with poly(ethyleneimine) (FND@PEI) [17,19]. Using our automatized biodistribution pipeline, we map the Cop⁺-FND:siRNA bioavailability and quantify its tissue distribution *in vivo* after systemic intravenous (i.v.) injection. Following the results of this injection, we design a new therapeutic strategy, relying on intra-tumoral (i.t.) administration, leading to efficient inhibition of the oncogene. Our results demonstrate that the automated quantitative biodistribution method we developed for FND injected in mice, is a valuable tool to design a therapeutic strategy. We show that it can also provide insights on nanodiamond cellular fate and elimination pathways thanks to its sub-cellular resolution and high sensitivity of nanoparticle detection.

2. Results and Discussion

2.1. Cop⁺-FND:siRNA optimal design and its oncogene inhibition efficacy in human Ewing Sarcoma cultured cells

In early studies, we used FND@PEI to deliver siRNA to cultured ES cells and we obtained a significant reduction of the expression of the oncogene responsible for the cell proliferation [17,18]. Here we replaced this strategy with Cop⁺-FND, a new generation of a cationic copolymer interface covalently grafted from the FND surface (the exact composition of the copolymer used in this study is the result of a thorough investigation which will be reported in a separate communication).

We first investigated the size and charge of this novel Cop⁺-FND:siRNA complex. To obtain robust data, we independently synthesized three different batches of Cop⁺-FND and analyzed their colloidal properties. The samples showed a great batch-to-batch reproducibility with narrow distribution of Z-average diameter 128.2 ± 8.7 nm (measured by dynamic light scattering, DLS), an apparent ζ -potential of 46.0 ± 3.7 mV (measured by electrophoretic light scattering, ELS), and sample conductivity 4.2 ± 1.8 μ S/cm in nuclease free water (pH 5.1). All these values are mean \pm standard deviation, over the three independent batches, and the measurement procedure for one batch is described in the Experimental Section.

For the siRNA, we considered a siRNA sequence directed against *EWS-FLI1* junction oncogene (siAS), as in our previous work [17,18,22]. This oncogene is involved in the vast majority of Ewing sarcoma, a young adult bone and soft tissue cancer [23] with bad prognosis. To get an optimal Cop⁺-FND:siAS mass ratio, the apparent ζ -potential of the complex must stay positive after siRNA binding. We chose a mass ratio as low as possible, but still preserving the colloidal stability. Using siAS we determined the optimal Cop⁺-FND:siAS mass ratio to be 25:1 by varying the amount of Cop⁺-FND at a fixed concentration of siAS in water at 25°C. Formation of Cop⁺-FND:siAS complex from Cop⁺-FND in water led to a slight increase of the Z-average diameter to 150.9 ± 6.2 nm and a decrease of the apparent ζ -potential down to 38.4 ± 0.8 mV, due to charge compensation (**Table S1** and **Figure S1**, Supporting Information).

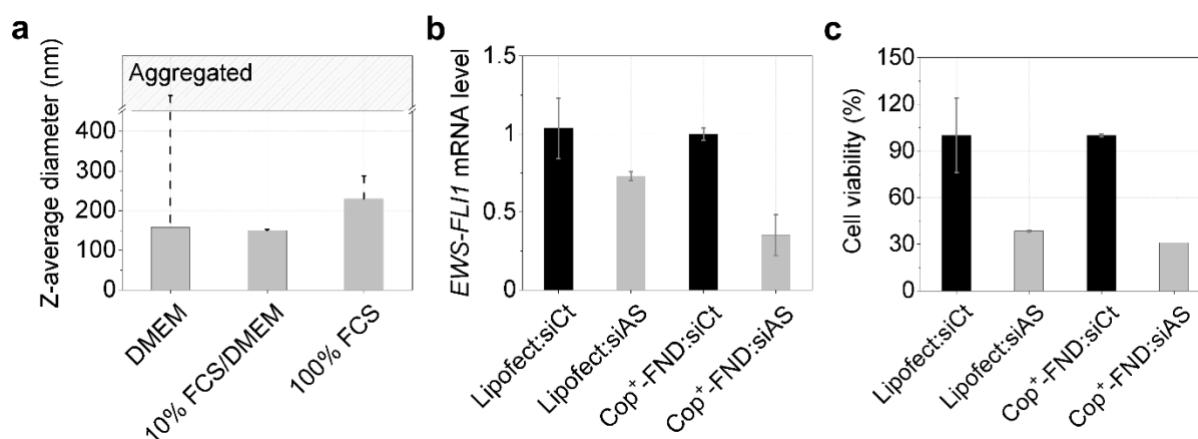


Figure 1. Cop⁺-FND:siRNA conjugate characterization: size and *in vitro* oncogene inhibition efficacy. a) Hydrodynamic size (Z-average) measurement by DLS of the Cop⁺-FND:siAS

complex at a diamond:siRNA mass ratio of 25:1, in different medium conditions at 37 °C (Inset: scheme of the complex). All measurements were done with Cop⁺-FND batch #1 and repeated ten times (during approximately 20 min). Each bar represents the first measurement and the top part of the superimposed dashed line the 10th one. More detailed data (raw DLS intensity autocorrelation functions and intensity size distributions) are shown in Table S1 and Figure S1, of the Supporting Informations. b) *In vitro* inhibition of *EWS-FLII* mRNA expression in A673 ES cells in culture, using 100 nM siRNA. Measurement by RT-qPCR, 48 h post-treatment. c) Inhibition of the proliferation of A673 cells measured 72 h post-treatment.

Then, after Cop⁺-FND:siAS formation in water at 25°C, we tested its colloidal stability in serum free DMEM, 10% and 100% FCS at 37 °C (**Figure 1a**). While the diluted FCS reveals a stabilization effect thanks to the presence of serum proteins, serum free DMEM strongly destabilizes the particles leading to rapid aggregation [24]. Adsorbing serum proteins in 100% FCS caused an almost two-fold increase of the diameter and a slow aggregation (**Table S1** and **Figure S1**, Supporting Information).

We then measured the inhibition efficacy of the siAS vectorized by Cop⁺-FND in A673 human Ewing sarcoma cells in culture. After a 48 h incubation with the Cop⁺-FND:siAS, *EWS-FLII* messenger RNA (mRNA) was extracted and its fraction was measured compared to a reference by RT-qPCR. **Figure 1b** shows that *EWS-FLII* expression in A673 cells treated with Cop⁺-FND:siAS (25:1 mass ratio) was specifically inhibited compared to a treatment with an irrelevant siRNA (siCt), and to the siAS delivered by Lipofectamine 2000. Inhibition of *EWS-FLII* was followed by a proliferation capacity of A673 cells decreased to 31%, compared to the cell viability observed in cells treated with Cop⁺-FND:siCt (**Figure 1c**). Moreover, *EWS-FLII* inhibition is dependent on siAS concentration. In an additional separate experiment we demonstrated 25% inhibition at 30 nM siRNA and 90% for 150 nM siRNA when Cop⁺-FND:siAS (65:1 mass ratio) was used in the presence of serum in the transfection media (**Figure S2**, Supporting Information). The capacity of Cop⁺-FND to deliver an efficient siRNA to cells in a serum containing medium is a superior advantage for the animal studies we then carried out.

Interestingly, our experiments also showed that the optimal Cop⁺-FND:siAS mass ratio providing stable colloidal sample depends on the content of salt impurities which differs between siRNA suppliers. We repeatedly obtained the optimal mass ratio 25:1 with siRNA purchased from Sigma Aldrich. Improperly purified siRNA lead to an increase of the Cop⁺-FND:siRNA mass ratio to 65:1 to maintain colloidal stability; biological activity was unaffected (**Figure S2**, Supporting Information). Compared to the optimal estimated ratio of 140:1 in the case of FND@PEI [17], these results indicate that Cop⁺-FND has a much larger binding capacity to carry siRNA.

2.2. High-resolution automatic quantification of Cop⁺-FND:siRNA in mouse organ sections after intravenous injection

To evaluate the siRNA therapeutic strategy *in vivo* we xenografted an Ewing sarcoma cells tumor in mice, and we first considered i.v. administration of the Cop⁺-FND:siAS. The siRNA delivery efficacy in animals is largely dependent on nanoparticles distribution after administration in blood circulation. Because no specific targeting is associated to Cop⁺-FND, they are expected to be captured by all cells having endocytosis capacities. However, Z-average size of Cop⁺-FND:siAS, smaller than 300 nm, lies in the range where the enhanced permeability and retention (EPR) effect [25] may allow them to extravasate from the tumor blood vessels into the tumor microenvironment, leading to their larger accumulation in the tumor. We decided to measure the main organ and tumor FND distribution at high sensitivity and spatial resolution. To this aim we developed an automated quantitative biodistribution measurement pipeline relying on time-gated widefield detection of FND in histological tissue sections.

2.2.1. Automated quantification of FND in histological tissue sections

Large-scale high-resolution image acquisition with a home-made time-gated microscope: The heart, the liver, the kidneys, the lungs, the spleen and the tumor were collected in two mice

sacrificed 24 hours after i.v. injection, sectioned (4 μm thick), and inserted between a coverslip and a microscope slide for imaging with a home-made time-gated wide field fluorescence microscope, described in details the Experimental section. Briefly, this setup relies on an inverted fluorescence microscope automatic slide scanner, in which we inject the beam of a home-made pulsed laser (wavelength 532 nm) shaped for widefield illumination synchronized with the delayed-detection via an intensified CCD (ICCD) array detector (**Figure 2a**).

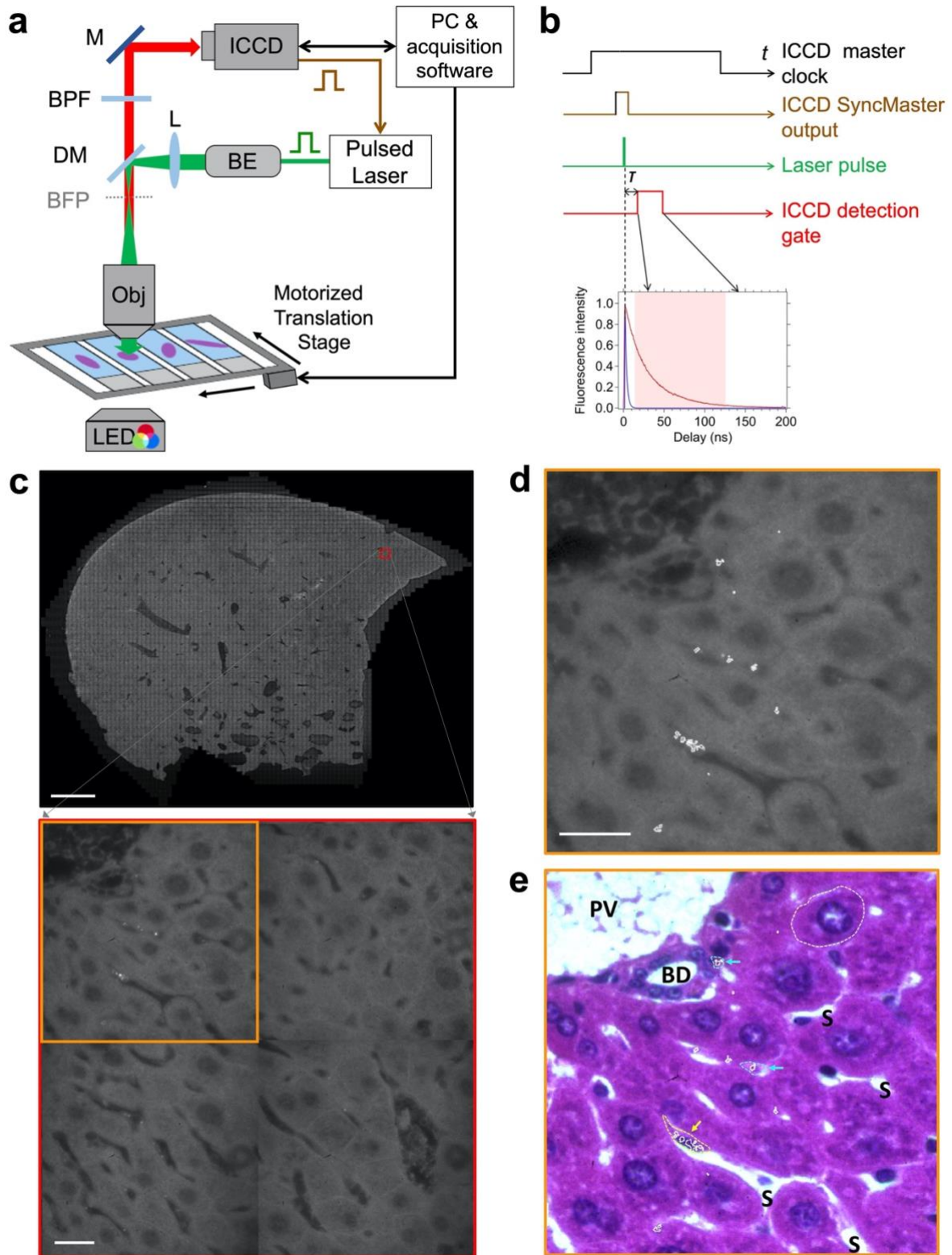


Figure 2. Automatised time-gated fluorescence and bright-field microscopy setup to screen nanodiamond in mouse organ sections with subcellular resolution. a) Motorized epifluorescence microscope equipped with a slide holder containing up to 4 slides with organ section preparations. BE: beam expander; DM: dichroic mirror; L: lens; BFP: microscope objective back focal plane; BPF: bandpass filter; ICCD: intensified charge coupled device array detector. internal clock. b) Chronogram of the acquisition sequence. ICCD clock signal

(SyncMaster Output) serves as a master to triggers the laser pulse. The fluorescence detection takes place with an adjustable delay relative to the pulse emission, and during a given gate duration (light red shaded area in the fluorescence decay curve). For each field of view, a brightfield image is also acquired on the same array detector, from three consecutive illuminations by a red, blue and green LED integrated in a condenser. A motorized translation stage, controlled by the acquisition software, ensures the motion from one field of view to the adjacent one, as well as from one slide to the next one. The areas covered by the organ slices in each slide, and a set of focus landmarks, have to be defined prior to the acquisition, which is then fully autonomous. c) Top: mosaic of 6500 field-of-view (FOV) of fluorescence images acquired from a HES-stained liver section. Scale bar: 1 mm. Bottom: zoom on 4 adjacent FOV of a region framed in red. The FOV surrounded by an orange frame displays bright spots corresponding to FND. Scale bar: 20 μm . d) Regions of interest (ROI) where FND have been automatically detected are surrounded by a white line. Scale bar: 20 μm . e) Bright-field image (histopathology view) of the same FOV as in d), resulting from the composition of the three LED acquisitions. Cell nuclei appear darker. FND-containing ROI are superimposed like in d). The arrows point at cells containing FND. The two blue arrows point at what may be Kupffer cells while the yellow arrow point at an endothelial cell. S: sinusoids; BD: bile duct; PV: portal vein.

We delayed the detection by 15 ns from the laser excitation pulse, to strongly reduce the autofluorescence compared to the FND emission, which lasts one order of magnitude longer [15] (**Figure 2b**). A dedicated software drives the slide scanner displacements and image acquisitions, a single organ section coverage requiring the recording of up to 15,000 individual images (FOV of size $\approx 110 \mu\text{m}$ with a $\times 60$ oil-immersion microscope objective). The same software serves to stitch these individual images and form a ≈ 120 Mpixels high-resolution image (**Figure 2c**), containing the millimeter size whole section with a pixel resolution of 200 nm. Note that the intensifier phosphor of the ICCD limits the spatial resolution of the image, spreading photons on ≈ 3.3 pixels full-width at half-maximum (FWHM) according to the ICCD manufacturer specifications. If we convolute this spreading with (i) the diffraction limit of our optical system (240 nm FWHM, for 700 nm emission wavelength and 1.40 numerical aperture objective) and (ii) the FND size (≈ 50 nm) we get a point-spread function (spot of a single emitter in the recorded image) of ≈ 5 pixels FWHM in agreement with our experimental resolution.

Automatic detection of FND in organ section images: The detection and quantification of the Cop⁺-FNDs in the different organ sections were realized thanks to a dedicated image analysis pipeline. Briefly, small elements brighter than the mean image intensity were first identified in FND fluorescence channel, with a Top-hat filter, and a region of interest (ROI) identifier was assigned to each of them. This first image processing did not include any size differentiation, thus a filtering program for every organ has been developed, considering the residual autofluorescence level and the anatomy of each tissue, these parameters being different from one organ to the other (**Table S2**, Supporting Information). The result of this automatic detection can be seen in **Figure 2d** and in **Figure 3a,b** for other FOV in liver and tumor.

Furthermore, in order to have both histopathological information and Cop⁺-FND localization, some sections were stained with Hematoxylin/Eosin/Saffron (HES). In that case, a bright-field color image was also acquired in addition to the fluorescence one, using a red-blue-green collimated LED (**Figure 2e**). However, despite the time-gating modality that rejects short-lifetime emitted photons, HES staining lead to a too high level of auto-fluorescence, so that stained samples were only used to better understand cellular and sub-cellular localization of Cop⁺-FNDs as discussed in section 2.2.3.

2.2.2. FND tissue distribution: quantification and aggregation state

For the quantification of Cop⁺-FND organ distribution we only used non-stained sections. To ensure the detection of all FND in the whole depth of the 4 μm thick organ section, we acquire two images (350 ms duration each) at two focusing z depths 3 μm apart. Moreover, even with time-gating detection and absence of staining, the tissue auto-fluorescence could not be totally suppressed to discriminate single FND unambiguously from localized tissue autofluorescence. We therefore also added a bleaching step (same duration of 350 ms) before each z -plane acquisition. The bleaching step decreased the auto-fluorescence by about 40%, without affecting Cop⁺-FND signal, thanks to its perfect photostability. Overall, each FOV is recorded

four times. FND identification was then based on a z -projection (of the bleaching and of the following steps) and followed by a comparison of the relative intensity of FND candidate spots to the background, before and after the bleaching: only FND spots are expected to keep their intensity constant. **Figure 3a,b** left panel shows the raw image before ROI identifications in liver and tumor sections respectively, in which single and aggregated Cop⁺-FND appear as white spots, and the corresponding right images show a white line delineating the ROI around identified Cop⁺-FND.

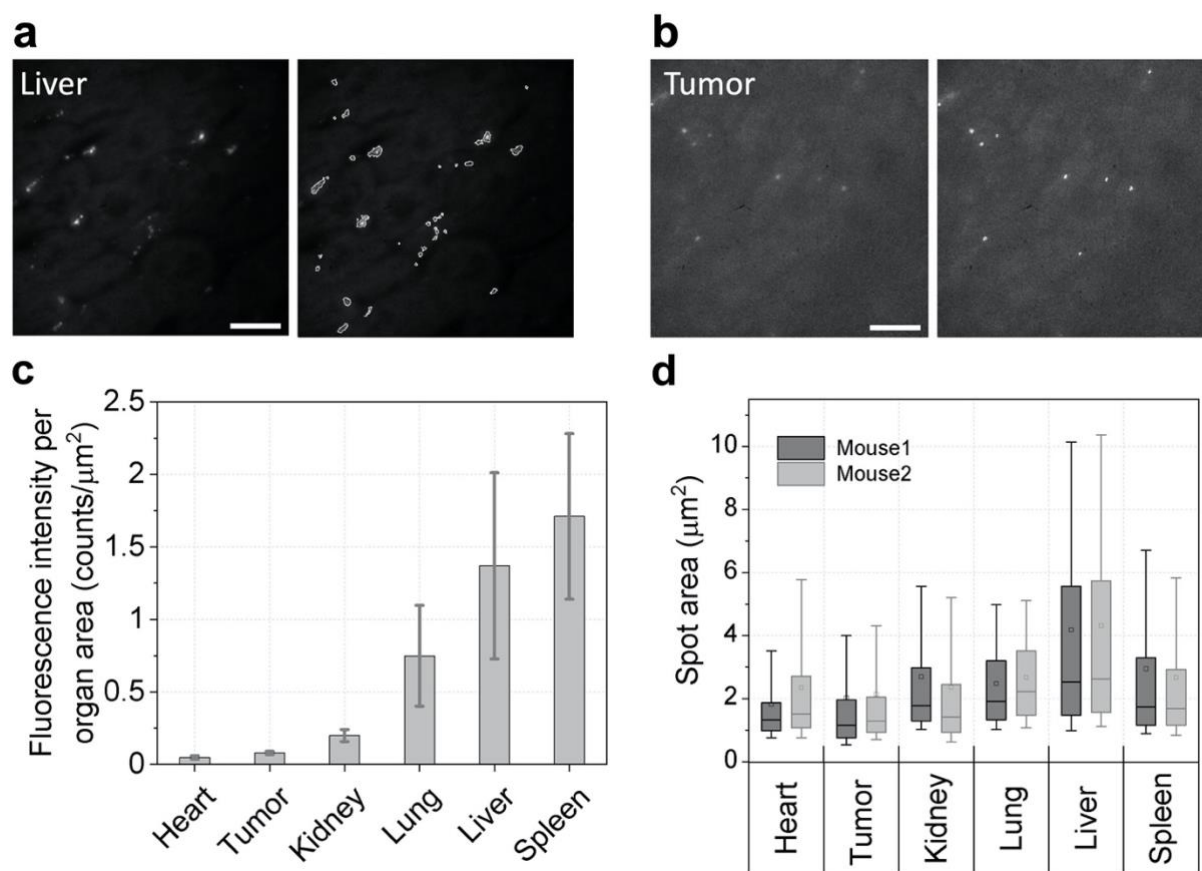


Figure 3. Automatic quantification of the amount of Cop⁺-FND and aggregation state in the different organ sections inferred from time-gated fluorescence imaging. a,b) One fluorescence FOV of a liver (a) and tumor (b) section without (left) and with (right) the ROI surrounding automatically detected FND. Scale bar: 20 μm . c) Total fluorescence intensity of all ROI detected divided by the surface of the organs. d) Distribution of the ROI areas in the different organs. The boxplot characterizes a sample using the 25th, 50th and 75th percentiles, and 90% and 10% whiskers; horizontal line in the box: median of the distribution; square: mean of the distribution. The outliers were not presented here. Data from $n=2$ organ sections from 2 mice.

Our automatic and high-throughput detection allowed to quantify the Cop⁺-FND in each organ, by extracting different parameters. The first one is the level of fluorescence intensity per

organ section area (**Figure 3c**), which is related to the number of Cop⁺-FND; it would be proportional to it if each single FND had the same fluorescence level, which is not the case. The organ section displaying the highest fluorescence intensity per unit area was the spleen (1.71 ± 0.57 count/ μm^2), closely followed by the liver (1.37 ± 0.64 count/ μm^2). The lung, which was the organ in which the largest number of ROIs was detected, comes third (0.75 ± 0.35 count/ μm^2). Finally, the kidneys (0.2 ± 0.04 count/ μm^2), the tumor (0.08 ± 0.01 count/ μm^2) and the heart (0.05 ± 0.01 count/ μm^2) presented much smaller accumulation of Cop⁺-FND. A second meaningful parameter is the ROI area representing the aggregation state of Cop⁺-FND shown on **Figure 3d**. Three groups can be distinguished. The one of the liver, which separates from the other organs by a median ROI size of 4.2 ± 3.9 μm^2 and a very large dispersion with a maximum at almost 11 μm^2 . The second group is made of the lung, spleen and kidney, having similar large ROI median sizes and dispersions of about 2.7 ± 2 μm^2 . The third group of organs in ROI area consists in the heart and the tumor, the latter presenting the lowest median value which indicates a minor aggregation state in this tissue. This might be the sign of a lower cellular uptake efficiency by the large macropinocytotic vesicles (size >1 μm) in tumors compared to other organs like the liver. In previous studies in cultured cells we have identified that the macropinocytotic compartments (as opposed to endosomal ones, sizes ≈ 100 - 500 nm) allowed the release of siRNA in the cytosol where these molecules are active [18,22].

The liver, kidneys and spleen are organs which function is to filtrate the blood and remove undesirable metabolites, xenobiotics and participate to the destruction of impaired blood cells. This function leads to all body blood filtration and may be responsible for the larger accumulation of nanoparticles. However, considering that Cop⁺-FND accumulates and aggregates also in the lung in addition to the filtration organs, one cannot exclude that the nanoparticle aggregation takes place in the blood stream, leading to Cop⁺-FND entrapment in alveolar capillaries. The broad distribution of ROI sizes in the lung is most probably due to the

diversity of sizes of capillaries. Regarding the tumor, our observation of a low accumulation is in agreement with a recent meta-analysis concluding that less than 1% in mass of nanoparticles administered systemically end up in the tumor target [26], but the fact that the amount found in the tumor is up to 17 fold smaller compared to the one found in the liver tends to contradict the EPR “passive” targeting effect of nanomedicine [25]. However, it has been pointed out that EPR is heterogeneous and can be affected by physiological and pathological effects [27]. Moreover, our observations have been done at a single time-point of 24 h after intravenous injection. Therefore, our data does not allow to discriminate between either an ineffective EPR effect, or a fast journey of the Cop⁺-FND through the tumor, thanks to a low aggregation state in this organ. Only additional experiments, at time points shorter than 24 h, would allow to conclude on the dominant phenomenon.

2.2.3. FND cellular localization in liver histological sections

To investigate in which compartments of the liver Cop⁺-FND end up, we then took advantage of high magnification of individual image constituting the mosaic and of the bright field acquisition of HES stained sections. **Figure 2e** shows examples of Cop⁺-FND ROI superimposed to HES images. FND were found in majority internalized in endothelial cells bordering the sinusoids, and second, most probably inside Kupffer cells. The latter are liver-resident macrophages part of the mononuclear phagocyte system and essential to maintain liver homeostasis and scavenge xenobiotics and cell debris [28]. A staining specific of macrophages like F4/80 [29] would allow to unambiguously distinguish Kupffer cells from endothelial cells, so that we could have an accurate quantification of each cell type. The capture by Kupffer cells, if it is confirmed, would not be favorable to the delivery of nanomedicine into the target tumor, but it is not the sole mechanism responsible for the low yield of nanoparticles ending up in tumor after systemic administration, as recently reported in models where Kupffer cells were

removed [30]. The interaction with other organs than the liver, like the spleen, need also to be tuned to achieve a larger tumor delivery.

Let us further point out that the phagocytosis of nanodiamonds by Kupffer cells was already reported a decade ago [10], and that these cells are expected to play an important role in the elimination of these particles from the organism. However, we did not detect any nanodiamond in hepatocytes 24 h after administration, which indicates that we either did not wait long enough for their passing from the Kupffer cells to the hepatocyte before reaching the bile duct and being eliminated in the feces, or that they are sequestered for a longer period and might not be eliminated at all. In any case, the important phagocytosis of the Cop⁺-FND by the Kupffer cells may reduce the bioavailability of the FND and could explain the low amount of Cop⁺-FND detected in the tumor after i.v. injection in the two mice used for the biodistribution study. Considering these results, to test the *in vivo* efficacy of Cop⁺-FND:siAS (siRNA targeting *EWS-FLII* oncogene) in animals we opted for intratumoral administration.

2.3. *In vivo* EWS-FLII inhibition efficacy by Cop⁺-FND:siAS injected intratumorously

For this *in vivo* efficacy experiment, we treated 6 athymic mice bearing A673 subcutaneous tumors with Cop⁺-FND:siAS complexes or with Cop⁺-FND:siCt bearing a control, non-specific, siRNA. We used the same FND:siRNA preparation (mass ratio 25:1) as the one applied to *in vitro* experiment that showed high inhibition efficacy (**Figure 1c**). In the *in vivo* experiment, mice were sacrificed 48 h post-FND intratumoral administration and the expression of *EWS-FLII* oncogene in tumors was measured by RT-qPCR. We observed a 28-fold decrease of *EWS-FLII* mRNA levels in tumors treated with Cop⁺-FND:siAS with respect to the tumors treated with siCt (**Figure 4a**), indicating that Cop⁺-FND efficiently delivered and released the therapeutic siRNA. Moreover, at the protein level, Cop⁺-FND:siAS treated tumors showed a lower ($p=0.03$) nuclear EWS-FLII immuno-histo-chemical (IHC) staining than Cop⁺-FND:siCt (**Figure 4b,c**), except for one preparation over five which displayed an abnormal IHC

labeling intensity distribution (**Figure S3**, Supporting Information). These results support the fact that Cop⁺-FND:siAS is able to efficiently deliver siRNA *in vivo* and that intratumoral administration of this type of nanomaterials could offer therapeutic advantages over alternative delivery systems such as Lipofectamine.

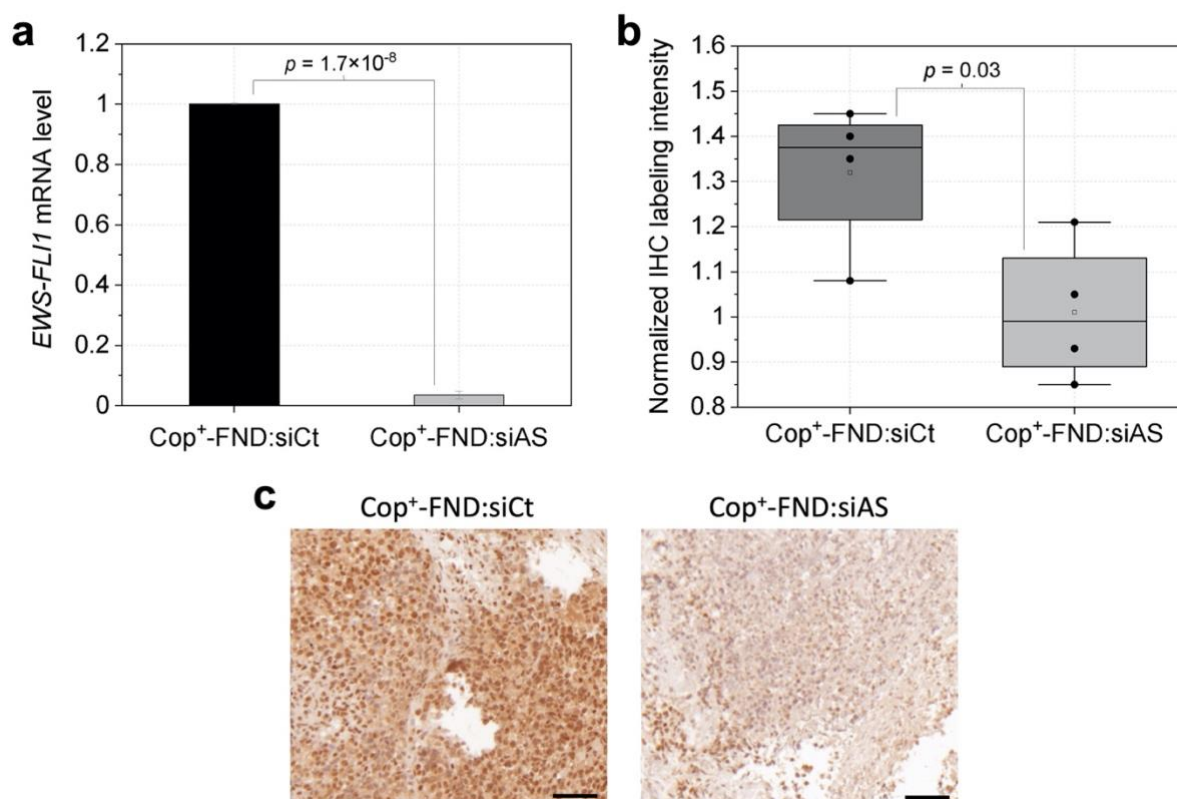


Figure 4. *In vivo* efficacy of Cop⁺-FND:siRNA in subcutaneous A673 xenografts 48 h after intratumoral administration. Cop⁺-FND:siRNA mass ratio of 25:1. a) *EWS-FLI1* mRNA expression levels in tumors treated either with a siRNA directed towards *EWS-FLI1* (siAS) or with the control siRNA (siCt); $n=6$ mice per group. b) Quantification of *EWS-FLI1* IHC cell nucleus intensity from 4 mice (one tumor section per mouse) in each group, displayed as boxplots: the middle bar is the median, the empty square is the mean, and circles are values of each section. c) Examples of bright field microscopy images of IHC preparations (siCt and siAS treatments) used for *EWS-FLI1* protein expression quantification reported in b). Scale bars: 50 μ m.

We recently reported that 7 nm sized detonation nanodiamonds (DNDs), rendered cationic by hydrogenation, can deliver an efficient siAS to mice bearing the same xenografted Ewing sarcoma tumor, after intravenous injection [31]. We observed a two-fold decrease (50% inhibition) of *EWS-FLI1* mRNA levels in tumors of mice treated with DND:siAS compared to mice treated with DND:siCt. As one could have expected, this efficacy is much lower than the

one we achieved here by intratumoral injection. In the same work using DND, we also investigated the nanodiamond tissue distribution after their radiolabeling with tritium (in replacement of hydrogen) and i.v. injection. A similar distribution as for Cop⁺-FND:siRNA was found, with the liver first, then the lungs and the spleen being the organs with the largest concentration of nanodiamonds. DND were also found in the feces but not in urine, which led us to the hypothesis that they could be eliminated in the bile through liver filtration. However, the tritiated DND could only provide whole organ-scale measurements and we could not spatially resolve their cellular fate, contrary to the experiments reported here using individually traceable FND (**Figure 2e**).

3. Conclusion

We investigated the extension to *in vivo* of our early *in vitro* experiments in which we showed that fluorescent nanodiamonds can transport siAS molecules inhibiting efficiently Ewing sarcoma *EWS-FLII* oncogene in cultured cells [17]. We first evaluated the FND bioavailability after intravenous injection. To this aim, we took advantage of the intense emission of FND, their absence of photobleaching and their fluorescence lifetime which is one order of magnitude longer than the one of tissue autofluorescence, to build an automated imaging and detection pipeline. The latter provides high-resolution (≈ 120 Mpixels) fluorescence and histological images with single-particle and subcellular resolutions. Moreover, we also used an improved cationic functionalization of FND, that no more relies on physisorption of PEI [17,18], but on a cationic copolymer grafted covalently from FND surface forming Cop⁺-FND nanoconjugates. This novel vector enabled to transport siAS efficiently into human Ewing Sarcoma cultured cells, and lead to a stronger inhibition of *EWS-FLII* junction oncogene of 90% compared to the 55% previously obtained with physisorbed cationic polymer [17]. We then measured, with our custom imaging and quantification procedures, the main organ and tumor distribution of Cop⁺-FND 24 h after i.v. injection of Cop⁺-FND:siAS. We found Cop⁺-FND in all tissues

investigated but with large differences of concentrations, and in particular a low one in the tumor. The dominant accumulation was in liver, spleen and lungs, as reported for other types of nanoparticles (administered intravenously to mouse for the same purpose) with similar size and surface charge [32], suggesting that this distribution might be driven by these basic physicochemical properties and not by chemical specificity. Our high spatial resolution imaging also allowed us to resolve individual Cop⁺-FND from aggregated ones, and the lowest aggregation state was found in the tumor. This might reveal a preferential uptake by endocytosis, while we previously showed that micropinocytosis is the main pathway for the delivery of an active siRNA in the cytosol [18,22]. Based on these tissue bioavailability measurements, we decided for the *in vivo* therapeutic efficacy study to inject the Cop⁺-FND:siAS directly in the tumor. We did observe, 48 h after injection, a large (28-fold) decrease of *EWS-FLI1* mRNA content in siAS treated tumor compared to control, translating in a decrease in EWS-FLI1 content in the tumor. The method we developed and reported here to determine the tissue bioavailability of fluorescent nanodiamonds by automated time-delayed high-resolution fluorescence microscopy, can be extended to other luminescent nanoparticles with emission lifetimes up to ~100-200 ns, like near-infrared emitting quantum dots [33]. Longer lifetimes would require to increase the pulse laser repetition period beyond 1 μ s, to avoid to filter-out legitimate photons. This would then require to increase the image pausing duration, in order to keep the photon counts constant, and the total acquisition time will increase beyond what is practically acceptable. Our method is therefore better suited for emission lifetime in a range of 50-200 ns. Finally, the ICCD could also be used in a dynamic mode to investigate the motion of FND-labelled subcellular compartments in live tissue sections, extending to thick samples studies carried-out in cultured cells [34].

4. Experimental Section and Methods

Cop⁺-FND synthesis: Commercially available diamond nanocrystals (MSY 0-0.05, Microdiamant, Switzerland) obtained from milling High Pressure High Temperature nanodiamonds (type Ib, with nitrogen impurity concentration of ≈ 200 ppm) were oxidized by air in a furnace at 510 °C for 4 h and treated with a mixture of HF and HNO₃ (2:1) at 160°C for 2 days. The particles were washed with water, 1 M NaOH, 1 M HCl and water. NV centers were created in the nanodiamonds according to the published protocol [35]. Briefly, NDs were irradiated with a 16.6 MeV electron beam to obtain a high density of vacancies, annealed at 900°C (1 h) to create NV centers and oxidized by air (510°C for 4 h). The resulting powder was again treated with a mixture of HF and HNO₃ and then washed with NaOH, HCl and water. This procedure eventually provided an aqueous colloidal solution of fluorescent ND. FND colloid (60 mL, 2 mg/mL) dissolved in purified water (Milli-Q, Millipore, USA) was used for coating with methacrylate-terminated thin silica shell (hydrated SiO₂) [36,37] using a modified Stöber procedure [38]; amount of all components needed for silication was linearly recalculated to amount of FND (120 mg). Terminal methacrylate groups of the silica shell were used to grow a dense layer of copolymer via radical polymerization. The resulting Cop⁺-FND samples were centrifuged five times and dissolved in nuclease free water to the final concentration of 9 mg/mL. The samples were stored at -20 °C in MeOH for long-term storage or in nuclease free water at 4°C for biological and stability testing.

siRNA sequences and Cop⁺-FND:siRNA complexation: We ordered two custom MISSION[®] siRNA desalt from Sigma Aldrich (USA): siRNA directed toward *EWS-FLII* (siAS), and a control irrelevant siRNA (siCt). The siAS sense strand sequence was: GCA GCA GAA CCC UUC UUA Ud(GA); the siAS antisense strand was : AUA AGA AGG GUU CUG CUG Cd(CC)). The siCt sense strand was: CGU UAC CAU CGA GGA UCC Ad(AA); the siCt antisense strand: UGG AUC CUC GAU GGU AAC Gd(CT)). Before complexation with siRNA, the Cop⁺-FND solution was sonicated for 15 s in an ultrasonic bath. Then, the diluted

Cop⁺-FND solution was added to the diluted siRNA solution at a mass ratio 25:1 of Cop⁺-FND:siRNA, and the mixed solution was put again in the ultrasonic bath for 20 s. This protocol, and more particularly the mass ratio, has been optimized to provide very stable colloidal suspensions and to strongly limit aggregation at all stages of the complex formation. The success of the complexation step was characterized by a clear and translucent final suspension, while a failure resulted in a milky dispersion that flocculates.

Nanoconjugates colloidal stability as evaluated by DLS and ELS: Z-average diameter and apparent ζ -potential were measured with a Zetasizer Nano ZSP (Malvern Instruments, UK) equipped with a He-Ne laser emitting a power of 10 mW at 633 nm wavelength. Scattered light was collected at the backscatter angle of 173°. Apparent diffusion coefficient was calculated from the fit by the first cumulant of a 3rd-order cumulant analysis (using Zetasizer Software 7.11, Malvern Instruments, UK) of $G^{(2)}(\tau)-1$, where $G^{(2)}(\tau)=\langle I(t)I(t+\tau) \rangle_t$ ($\langle \cdot \rangle_t$ denoting time average) is the second-order time intensity autocorrelation function. Z-average diameter was inferred from this fit using the Stokes-Einstein equation. Size distributions displayed in Figure S1a, result from the non-negative least square analysis of Zetasizer Software 7.11. Unless stated otherwise, measured samples were diluted by UltraPure™ DNase/RNase-Free Distilled Water (Nuclease free water, Thermo Fisher Scientific, pH 5.1, conductivity \approx 250 μ S/cm) at 25°C with the final volume 0.6 mL (disposable cuvette); dynamic viscosity was set at 0.887 cP. Each sample was measured two times with an automatic duration; reported size diameters represent an average value of these measurements. Cop⁺-FND:siAS sample tested in DMEM, 10% FCS (DMEM cell culture media) and 100% FCS at 37 °C with the final volume 60 μ L (quartz cuvette ZEN2112) was measured ten times (total duration \approx 20 min); dynamic viscosity of the DMEM, 10% FCS (DMEM cell culture media) and 100% FCS at 37 °C was set at 0.726 [40], 0.738 [40] and 0.861 cP [41], respectively. ELS with a phase analysis of scattered light at forward angle of 13° was used for determination of the apparent ζ -potential.

The samples were measured in nuclease free water (pH 5.1) using monomodal analysis, two measurements with twenty subruns; To calculate the apparent ζ -potential value from Henry's equation [42] we have used Smoluchowsky approximation assuming value of the Henry's function 1.5 [42,43]. For both types of measurement, the particle concentration was below 0.2 mg/mL; dilution of the solvent by testing sample was always lower than 5%.

In vitro inhibition of EWS-FLII oncogene expression: Human Ewing carcinoma cells A673 were seeded at 2.5 to 5.10^4 cells/mL on a 24-wells plate or 6-wells plate (proliferation assay and RT-qPCR assay, respectively) in DMEM medium (Gibco) containing 10% bovine calf serum and 1% penicillin/streptomycin (Gibco) and incubated at 37°C , 5% CO_2 in moistly atmosphere one day before treatment. The medium was then replaced by $450\ \mu\text{L}$ of same medium plus $50\ \mu\text{L}$ of 10 mM HEPES pH 7.2, 100 mM NaCl containing Cop⁺-FND bound to either siAS or siCt (100 nM per well). The Cop⁺-FND:siRNA mass ratio was 25:1. A positive control was also tested, by using Lipofectamine 2000 (Invitrogen, USA) to deliver siRNA. Transfection was conducted in serum-reduced medium (Opti-MEM, Gibco, USA), during the first 4 h of incubation before to be replaced by DMEM containing 10 % bovine calf serum and penicillin streptomycin. To determine the cellular proliferation, the cells were counted 72h post-treatment comparing the different treatments. On the other hand, cells were incubated for 48 h to extract the total RNA by RNeasy RNA extraction kit (Qiagen, Spain), according to manufacturer's instructions. The total extracted RNA was dissolved in $10\ \mu\text{L}$ of water and RNA concentration was determined by spectrophotometry at the wavelength of 260 nm (Nanodrop, Thermo Fisher Scientific, USA). The reverse transcription was performed with $3\ \mu\text{g}$ RNA using High-capacity cDNA reverse transcription kit (ThermoFisher Scientific, CA, USA) according to the manufacturer's instructions. PCR quantification was carried out with $1\ \mu\text{L}$ of cDNA using SYBR-green PCR Master mix (Applied Biosystems, ThermoFisher Scientific). In detail, the *EWS-FLII* gene was amplified with the *EWS*- forward primer: 5'-AGC AGT TAC TCT CAG

CAG AAC ACC -3' and *FLII*-reverse primer: 5'-CCA GGA TCT GAT ACG GAT CTG GCT G-3' (Invitrogen). over 40 cycles, in a thermal cycler equipment (7500 Real-Time PCR system, Applied Biosystems, USA), as follows: 20 s at 95°C, followed by 40 cycles of 95°C for 15 s, 60°C for 30 s. The human *GAPDH* gene was used as control (forward primer: 5'- ACC CAC TCC TCC ACC TTT GAC -3', and reverse primer: 5'- CAT ACC AGG AAA TGA GCT TGA CAA-3'). Analysis of the expression levels of the genes of interest using QbasePLUS 2.0 software (Biogazelle, Belgium) and comparative CT (threshold cycle) methods was used to normalize the target CT by the *GAPDH* control gene CT ($2e^{-\Delta\Delta CT}$) [44].

Time-gated fluorescence microscope: The automated slide scanner setup relies on a first generation of the Pathfinder™ (Imstar S.A., France) slide scanner, composed of an epifluorescence inverted microscope (Eclipse Ti-E, Nikon, Japan) with a customized motorization (Imstar). For the fluorescence illumination in a pulse regime, we built our own laser system based on a modulated laser diode at 1064 nm wavelength amplified in a Nd³⁺:YVO₄ crystal, following our previously published design [45]. We slightly modified this design to achieve sub-nanosecond (≈ 100 ps) pulse duration. Before being injected into the microscope, the output beam was first frequency doubled using a non-critical phase matching lithium triborate crystal (LBO-405, Eksma, Lithuania) placed in an oven (NCPM-405, Eksma) set at a temperature of 149°C, for the efficient nonlinear production of 532 nm wavelength light. Then, the laser beam was $\times 10$ enlarged by a beam expander, reflected by a dichroic mirror (DM, z532rdc, Semrock, USA) and focused to the back focal plane of the microscope objective (oil immersion, Nikon Plan Apo $\times 60$, numerical aperture 1.40), to produce a ≈ 100 μm diameter illumination spot. The fluorescence from FND was detected through the DM and after the elimination of residual excitation laser with a bandpass filter (697/75 nm, Semrock). For the time-delayed imaging we used an intensified CCD array detector (ICCD PI-MAX3-1024i-18 mm-Gen-III-HBf-P46, Princeton Instrument, USA) which maximal 1 MHz internal clock

frequency (SyncMaster output) serves as the master for the time-delayed recording. Imstar Pathfinder™ software was adapted to drive this ICCD and pass it the desired parameters. The latter include the delay between the clock front edge and the intensifier gate opening (set to 15 ns), the gate duration (110 ns), the intensifier gain (set to 5) and the number of gates before the detector reading (corresponding to a total pausing duration of 350 ms). Considering the delays in the cables and laser drivers electronic circuit, each ICCD clock front edge synchronization signal was delayed (and also reshaped in 50-ns TTL pulses) with a pulse Pulse Generator Delay apparatus (TGP110, Aim-TTi, UK, not displayed on Figure 2a) so that it triggers a laser pulse exactly one period later (*i.e.*, 1 μ s later).

Cop⁺-FND:siRNA organ distribution: Nude mice were used for this assay, in accordance with the ethical project submitted and approved by the ethical committee regulating the animal facility at Gustave Roussy Institute (Villejuif, France). The mice were injected subcutaneously with $5 \cdot 10^6$ A673 cells, on one flank, and treatment was not begun until the tumor had reached a volume of 200 mm³. After reaching this point, 200 μ L of Cop⁺-FND:siRNA, according to the protocol described beforehand, were injected intravenously in the mouse's caudal vein with a final siRNA concentration of 1 mg/kg and a Cop⁺-FND:siRNA mass ratio of 25:1. Mice were sacrificed 24 h after the injection, by cervical dislocation in accordance with ethical procedures. Heart, lungs, liver, spleen, kidneys and tumor were collected and stored in FineFIX solution (Milestone srl, Italy), then embedded in paraffin and sectioned (thickness \approx 4 μ m). Sections were either let without any staining or colored with Hematoxylin/Eosin/Saffron (HES) solution. Sections of organs were then observed under a 60 \times magnification and 1.4 numerical aperture oil immersion microscope objective from the "home-made" time-gated fluorescence microscope. Fluorescence and bright-field image of the entire organ were acquired under the form of a mosaic of fields of view, of size \approx 110 \times 110 μ m each. The pausing duration for fluorescence was 350 ms, with a photocathode gain of 5, and a laser excitation power of 25 mW.

The mosaic of the entire organ section was reconstructed using Imstar Pathfinder software. It was then possible, by zooming into the reconstructed image, to observe the whole organ section at subcellular resolution. Finally, the motorized microscope stage accommodates a 4-slides charger mount so that we could launch the fully automatized acquisition of 4 organ sections at once. Overall, we could acquire an entire organ section (size between 25 and 110 mm²) in 6 to 10 hours.

Automatic image processing for FND identification: To detect FNDs, we first applied a Tophat transformation to the fluorescence signal image; this procedure effectively removes the background inhomogeneities. In the second step we measured the variation of each pixel intensity value below the image median value was calculated from the Tophat image; the detection threshold was set as the median plus the standard deviation multiplied by a fixed factor. The ROIs generated by the previous step were filtered according the following criteria, and only the ROIs passing all the filters were retained:

- (i) Global contrast: Value of the ratio between the ROI's average fluorescence intensity and the fluorescence intensity mode of the whole field of view. This parameter can be associated to the contrast of the ROI compared to the global image. The ROIs were considered as FNDs candidates only within a certain range of global contrast values;
- (ii) Local contrast: ratio of the ROI's average fluorescence intensity to that of a small ring (few pixels) around the ROI. This allowed to eliminate the ROIs with sufficiently high average fluorescence level but low local contrast; these were most probably false positives;
- (iii) Value of the total (integral) intensity of the object detected: below a specific threshold value, ROIs were considered as false positives;
- (iv) Area of the ROI: set to prevent the detection of a large part of the organ. In lung for instance, some parts of the organ were highly fluorescent and could be detected as FNDs if no size filter was applied;

(v) Ratio of the fluorescence intensity between the first bleaching step and the acquisition step. When this ratio was within a specific range, the detected ROIs were considered as FNDs (the fluorescence of FND does not decrease after the bleaching step).

The values of these filter parameters are provided in the Supporting Information Table S1.

In vivo efficacy: The *in vivo* efficacy assay was supervised and approved by the Animal Experimentation Ethical Committee at the Vall d'Hebron Research Institute and performed within the ICTS "NANBIOSIS" (www.nanbiosis.es/portofolio/u20-in-vivo-experimental-platform). In detail, six-week-old female nude mice ($n=20$) were subcutaneously injected with 5×10^6 A673 cells in the right dorsal back, and treatment was administered by a single injection when tumors reached approximately 75 mm^3 . The Cop⁺-FND:siRNA complexes (FND:siAS or FND:siCt) were assembled just before of the intratumoral (i.t.) administration of 20 μL of Cop⁺-FND:siRNA complex (mass ratio of 25:1). Animals were euthanized 48 h post-administration and tumors were processed for either frozen for later qPCR assays or fixed in 4% paraformaldehyde and embedded in paraffin for histological analysis. Both siRNA directed toward *EWS-FLI1* (same sequences as for the *in vitro* inhibition experiment) and control siRNA directed toward *FLUC2* (Forward primer: 5'-GGA CGA GGA CGA GCA CUU CUU-3'; reverse primer: 5'-GAA GUG CUC GUC CUC GUC CUU-3') were produced by Sigma Aldrich. The presence of EWS-FLI1 in tumor sections was analyzed by pre-treating paraffin-embedded formalin fixed sections with 100 mM citrate buffer (pH 6) in a pressure cooker. Sections were incubated with 10 % normal goat serum (NGS) in antibody diluent (1% BSA in Tris buffer 1X) and then of 1:50 dilution of anti-EWS-FLI1 antibody (MBS 300723, MyBiosource Inc., CA, USA). Secondary antibody consisted in a HRP conjugated system (EnVision+ System-HRP Labeled Polymer anti-rabbit from Agilent Dako, CA, USA), which was later visualized with diaminobenzidine colorimetric reagent solution (Agilent Dako) and counterstained with Harris hematoxylin (Sigma-Aldrich, MO, USA).

IHC quantification of EWS-FLI1: The quantification of EWS-FLI1 protein level in immunohistochemistry tumor sections was done using a pipeline from the Pathfinder software (IMSTAR S.A., Paris). The first step consists in color calibration of RGB images: the experimentalist selects about 10 positive (P) and negative (N) nuclei; in each image the software calculates at each pixel the optical density (OD, decimal logarithm of the ratio of a nucleus pixel intensity to the intensity of the non-nucleus background) of each color (OD_R , OD_G and OD_B , for red, green and blue respectively), normalizes it by $\sqrt{(OD_R^2 + OD_G^2 + OD_B^2)}$, and then extract the medians for N and P nuclei, resulting in 6 values: $C^{P,N}_R$, $C^{P,N}_G$ and $C^{P,N}_B$ for P and N. This calibration is performed once for given batch of IHC. The second step consists in decomposing the RGB image in P and N monochrome components defined by as: $OD_R = C^{P,R}_R \times P + C^{N,R}_R \times N$, for R and P case, and similar expression for G and B. P and N values can be seen as OD associated to the (C^P_R, C^P_G, C^P_B) and (C^N_R, C^N_G, C^N_B) colors respectively. In the third step the nuclei are segmented in both P and N images using an automated thresholding followed by watershed-based separation and resulting in nuclei ROI. Finally, the mean value of P is calculated for all nuclei ROI and the average intensity over all nuclei ROI located within the region of the tumor outlined by the pathologist is used as the measure of EWS-FLI1 protein level.

Acknowledgements

We are grateful to Dr. Xavier Sanjuan from Bellvitge Hospital and to Dr. Paule Opolon from Gustave Roussy Institute for their help in anatomopathological analysis; to Olivia Bawa from Gustave Roussy Institute for sample preparation; to Sandra Mancilla and Natalia García-Aranda from Vall d'Hebron Institut de Recerca for their technical assistance in immunohistochemistry and *in vivo* qPCR assays, and to Dr. David Chvatil from Institute of Nuclear Physics, Rez, for irradiation of nanodiamonds by electrons. This research was funded by the ERANET Euronanomed 2 program, through the French National Research Agency (ANR, grant number ANR-14-ENM2-0002 to F.T.) and through the Spanish Instituto de Salud Carlos III (ISCiii, grant numbers AC14/00032 to I.A. and AC14/00026 to O.T.M.); the Czech Science Foundation Project No.18-17071S (to P.C.); European Regional Development Fund, OP RDE, Projects: ChemBioDrug (No. CZ.02.1.01/0.0/0.0/16_019/0000729) (to P.C., M.K.) and CARAT (No.

CZ.02.1.01/0.0/0.0/16_026/0008382) (to P.C.). Irradiations were supported through MSMT project No. LM2015056 within the CANAM infrastructure of the NPI CAS Rez.

References

- [1] S. Kunjachan, J. Ehling, G. Storm, F. Kiessling, T. Lammers, *Chem. Rev.* **2015**, *115*, 10907–10937.
- [2] G. M. Thurber, K. S. Yang, T. Reiner, R. H. Kohler, P. Sorger, T. Mitchison, R. Weissleder, *Nat. Commun.* **2013**, *4*, 1504.
- [3] A. Hoffman, H. Manner, J. W. Rey, R. Kiesslich, *Nat. Rev. Gastroenterol. Hepatol.* **2017**, *14*, 421–434.
- [4] M. T. Matter, J. Li, I. Lese, C. Schreiner, L. Bernard, O. Scholder, J. Hubeli, K. Keevend, E. Tsolaki, E. Bertero, S. Bertazzo, R. Zboray, R. Olariu, M. A. Constantinescu, R. Figi, I. K. Herrmann, *Adv. Sci.* **2020**, *7*, 2000912.
- [5] G. A. Roth, S. Tahiliani, N. M. Neu-Baker, S. A. Brenner, *Wiley Interdiscip. Rev. Nanomedicine Nanobiotechnology* **2015**, *7*, 565–579.
- [6] E. D. SoRelle, O. Liba, J. L. Campbell, R. Dalal, C. L. Zavaleta, A. de la Zerda, *Elife* **2016**, *5*, DOI 10.7554/eLife.16352.
- [7] K. Turcheniuk, V. N. Mochalin, *Nanotechnology* **2017**, *28*, 252001.
- [8] H.-C. Chang, W. W.-W. Hsiao, M.-C. Su, *Fluorescent Nanodiamonds*, John Wiley & Sons, Ltd, Chichester, UK, **2018**.
- [9] G. Gao, Q. Guo, J. Zhi, *Small* **2019**, *15*, 1902238.
- [10] Y. Yuan, Y. Chen, J.-H. Liu, H. Wang, Y. Liu, *Diam. Relat. Mater.* **2009**, *18*, 95–100.
- [11] M. Radtke, E. Bernardi, A. Slablab, R. Nelz, E. Neu, *Nano Futur.* **2019**, *3*, 042004.
- [12] A. Hegyi, E. Yablonovitch, *Nano Lett.* **2013**, *13*, 1173–1178.
- [13] J.-J. Greffet, J.-P. Hugonin, M. Besbes, N. D. Lai, F. Treussart, J.-F. Roch, *arXiv.org* **2011**, *quant-ph*, 1107.0502.
- [14] S. Coda, A. J. Thompson, G. T. Kennedy, K. L. Roche, L. Ayaru, D. S. Bansi, G. W. Stamp, A. V. Thillainayagam, P. M. W. French, C. Dunsby, *Biomed. Opt. Express* **2014**, *5*, 515.
- [15] O. Faklaris, D. Garrot, V. Joshi, F. Druon, J. Boudou, T. Sauvage, P. Georges, P. A. Curmi, F. Treussart, *Small* **2008**, *4*, 2236–2239.
- [16] T. Wu, Y.-K. Tzeng, W.-W. Chang, C.-A. Cheng, Y. Kuo, C. Chien, H.-C. Chang, J. Yu, *Nat. Nanotechnol.* **2013**, *8*, 682–689.
- [17] A. Alhaddad, M.-P. Adam, J. Botsoa, G. Dantelle, S. Perruchas, T. Gacoin, C. Mansuy, S. Lavielle, C. Malvy, F. Treussart, J.-R. Bertrand, *Small* **2011**, *7*, 3087–3095.
- [18] A. Alhaddad, C. Durieu, G. Dantelle, E. Le Cam, C. Malvy, F. Treussart, J.-R. Bertrand, *PLoS One* **2012**, *7*, e52207.
- [19] M. Chen, X.-Q. Zhang, H. B. Man, R. Lam, E. K. Chow, D. Ho, *J. Phys. Chem. Lett.* **2010**, *1*, 3167–3171.
- [20] S. Agarwal, Y. Zhang, S. Maji, A. Greiner, *Mater. Today* **2012**, *15*, 388–393.
- [21] P. van de Wetering, N. M. E. Schuurmans-Nieuwenbroek, M. J. van Steenbergen, D. J. A. Crommelin, W. E. Hennink, *J. Control. Release* **2000**, *64*, 193–203.
- [22] J.-R. R. Bertrand, C. Pioche-Durieu, J. Ayala, T. Petit, H. A. Girard, C. P. Malvy, E. Le Cam, F. Treussart, J.-C. C. Arnault, *Biomaterials* **2015**, *45*, 93–98.
- [23] O. Delattre, J. Zucman, T. Melot, X. Sastre Garau, J.-M. Zucker, G. M. Lenoir, P. F. Ambros, D. Sheer, C. Turc-Carel, T. J. Triche, A. Aurias, G. Thomas, *N. Engl. J. Med.* **1994**, *331*, 294–299.

- [24] S. R. Hemelaar, A. Nagl, F. Bigot, M. M. Rodríguez-García, M. P. de Vries, M. Chipaux, R. Schirhagl, *Microchim. Acta* **2017**, *184*, 1001–1009.
- [25] H. Maeda, H. Nakamura, J. Fang, *Adv. Drug Deliv. Rev.* **2013**, *65*, 71–79.
- [26] S. Wilhelm, A. J. Tavares, Q. Dai, S. Ohta, J. Audet, H. F. Dvorak, W. C. W. Chan, *Nat. Rev. Mater.* **2016**, *1*, 16014.
- [27] H. Maeda, *Adv. Drug Deliv. Rev.* **2015**, *91*, 3–6.
- [28] L. J. Dixon, M. Barnes, H. Tang, M. T. Pritchard, L. E. Nagy, *Compr. Physiol.* **2013**, *3*, 785–97.
- [29] B. G. Lopez, M. S. Tsai, J. L. Baratta, K. J. Longmuir, R. T. Robertson, *Comp. Hepatol.* **2011**, *10*, 2.
- [30] A. J. Tavares, W. Poon, Y. N. Zhang, Q. Dai, R. Besla, D. Ding, B. Ouyang, A. Li, J. Chen, G. Zheng, C. Robbins, W. C. W. Chan, C. J. Murphy, *Proc. Natl. Acad. Sci. U. S. A.* **2017**, *114*, E10871–E10880.
- [31] S. Claveau, É. Nehlig, S. Garcia-Argote, S. Feuillastre, G. Pieters, H. A. Girard, J.-C. Arnault, F. Treussart, J.-R. Bertrand, *Nanomaterials* **2020**, *10*, 553.
- [32] H. Elhames, J.-R. Bertrand, J. Maccario, A. Maksimenko, C. Malvy, *Oligonucleotides* **2009**, *19*, 255–264.
- [33] S. Bouccara, A. Fragola, E. Giovanelli, G. Sitbon, N. Lequeux, T. Pons, V. Lorient, *J. Biomed. Opt.* **2014**, *19*, 051208.
- [34] S. Haziza, N. Mohan, Y. Loe-Mie, A.-M. Lepagnol-Bestel, S. Massou, M.-P. Adam, X. L. Le, J. Viard, C. Plancon, R. Daudin, P. Koebel, E. Dorard, C. Rose, F.-J. Hsieh, C.-C. Wu, B. Potier, Y. Herault, C. Sala, A. Corvin, B. Allinquant, H.-C. Chang, F. Treussart, M. Simonneau, *Nat. Nanotechnol.* **2017**, *12*, 322–328.
- [35] T. Rendler, J. Neburkova, O. Zemek, J. Kotek, A. Zappe, Z. Chu, P. Cigler, J. Wrachtrup, *Nat. Commun.* **2017**, *8*, 14701.
- [36] J. Slegerova, M. Hajek, I. Rehor, F. Sedlak, J. Stursa, M. Hruby, P. Cigler, *Nanoscale* **2015**, *7*, 415–420.
- [37] I. Rehor, H. Mackova, S. K. Filippov, J. Kucka, V. Proks, J. Slegerova, S. Turner, G. Van Tendeloo, M. Ledvina, M. Hruby, P. Cigler, *Chempluschem* **2014**, *79*, 21–24.
- [38] J. Neburkova, F. Sedlak, J. Zackova Suchanova, L. Kostka, P. Sacha, V. Subr, T. Etrych, P. Simon, J. Barinkova, R. Krystufek, H. Spanielova, J. Forstova, J. Konvalinka, P. Cigler, *Mol. Pharm.* **2018**, *15*, 2932–2945.
- [39] J. Neburkova, M. Hajek, I. Rehor, J. Schimer, F. Sedlak, J. Stursa, M. Hruby, P. Cigler, in *Methods Pharmacol. Toxicol.*, Humana Press Inc., **2017**, pp. 169–189.
- [40] R. Ahmad Khanbeigi, T. F. Abelha, A. Woods, O. Rastoin, R. D. Harvey, M.-C. Jones, B. Forbes, M. A. Green, H. Collins, L. A. Dailey, *Biomacromolecules* **2015**, *16*, 733–742.
- [41] O. Cakmak, C. Elbuken, E. Ermek, A. Mostafazadeh, I. Baris, B. Erdem Alaca, I. H. Kavakli, H. Urey, *Methods* **2013**, *63*, 225–232.
- [42] G. V. Lowry, R. J. Hill, S. Harper, A. F. Rawle, C. O. Hendren, F. Klaessig, U. Nobbmann, P. Sayre, J. Rumble, *Environ. Sci. Nano* **2016**, *3*, 953–965.
- [43] A. V. Delgado, F. González-Caballero, R. J. Hunter, L. K. Koopal, J. Lyklema, *J. Colloid Interface Sci.* **2007**, *309*, 194–224.
- [44] J. Hellemans, G. Mortier, A. De Paepe, F. Speleman, J. Vandesompele, *Genome Biol.* **2008**, *8*, R19.
- [45] X. Délen, F. Balembois, P. Georges, *Opt. Lett.* **2014**, *39*, 997.

Supporting Information

Harnessing subcellular-resolved organ distribution of cationic copolymer-functionalized fluorescent nanodiamonds for optimal delivery of therapeutic siRNA to a xenografted tumor in mice

*Sandra Claveau, Marek Kindermann, Alexandre Papine, Zamira V. Díaz-Riascos, Xavier Délen, Patrick Georges, Roser López-Aleman, Óscar Tirado Martínez, Jean-Rémi Bertrand, Ibane Abasolo, Petr Cigler, and François Treussart**

Table S1. Characterization of the colloidal properties of batch #1 of Cop⁺-FND and Cop⁺-FND:siAS complexes with a mass ratio 25:1 using DLS and ELS. Two first rows, all columns: mean \pm standard deviation of two measurements. Rows 3 to 5 (complex in specific medium): the size was measured ten times (during approximately 20 min). As indicators of colloidal stability, two values are displayed: 1st / 10th measurements. More detailed information about the measurement conditions can be found in the Experimental section.

	Z-average diameter [nm]	Apparent ζ -potential [mV]	Electrophoretic mobility [$\mu\text{m}\cdot\text{cm}/\text{V}\cdot\text{s}$]	Conductivity [$\mu\text{S}/\text{cm}$]	Applied voltage [V]
Cop⁺-FND (nuclease free water, 25 °C)	138.0 \pm 1.0	45.8 \pm 2.9	3.59 \pm 0.23	5.96 \pm 0.05	9.5
Cop⁺-FND:siRNA (siAS) (nuclease free water, 25 °C)	150.9 \pm 6.2	38.4 \pm 0.8	3.01 \pm 0.07	18.30 \pm 0.00	5.0
Cop⁺-FND:siRNA (siAS) (DMEM, 37 °C)	157.9 / aggregated	-	-	-	-
Cop⁺-FND:siRNA (siAS) (10% FCS, DMEM, 37 °C)	150.4 / 152.9	-	-	-	-
Cop⁺-FND:siRNA (siAS) (100% FCS, 37 °C)	229.9 / 287.7	-	-	-	-

Table S2. Ranges of the automatic detection parameters used to identify Cop⁺-FND in function of the organ considered. These parameters need to be adjusted to each type of organ due to large differences in their autofluorescence intensities.

	Global contrast	Local contrast	Total intensity [counts/350 ms per ROI]	Area [μm^2]		Ratio of intensity between bleaching and acquisition steps	
	min	min	min	min	max	min	max
Lung	1.3	1.2	30	0.25	7.5	0.65	1.25
Heart	0.8	1.27	20	0.4	9	0.75	1.25
Tumor	1.3	1.13	10	0.25	60	0.65	1.25
Liver	1.3	1.2	30	0.25	20	0.65	1.25
Spleen	1.3	1.2	30	0.25	20	0.65	1.25
Kidney	1.3	1.2	30	0.25	20	0.65	1.25

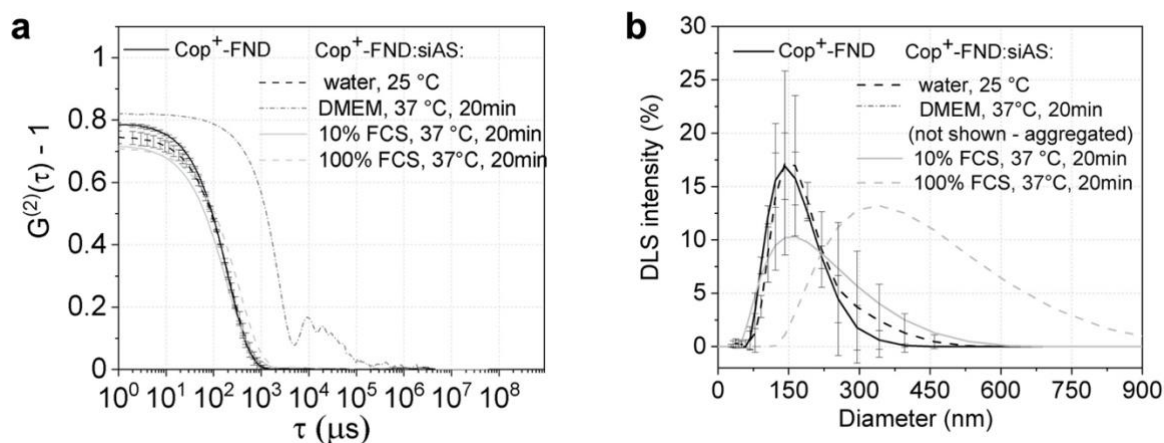


Figure S1. Size distribution of Cop⁺-FND and Cop⁺-FND:siAS of Table S1 samples (mass ratio 25:1). a) Raw DLS time intensity correlation functions $G^{(2)}(\tau)-1$. b) Intensity size distribution as inferred from the correlation data a), using non-negative least square analysis. In water at 25°C (dark grey dashed line) Cop⁺-FND:siAS size measurement was done twice and we report the average value \pm standard deviation. Cop⁺-FND:siAS in DMEM alone aggregated after 20 min. For Cop⁺-FND:siAS in DMEM with 10% FCS (conventional cell culture media) and in 100% FCS we display only the 10th measurement (after 20 min).

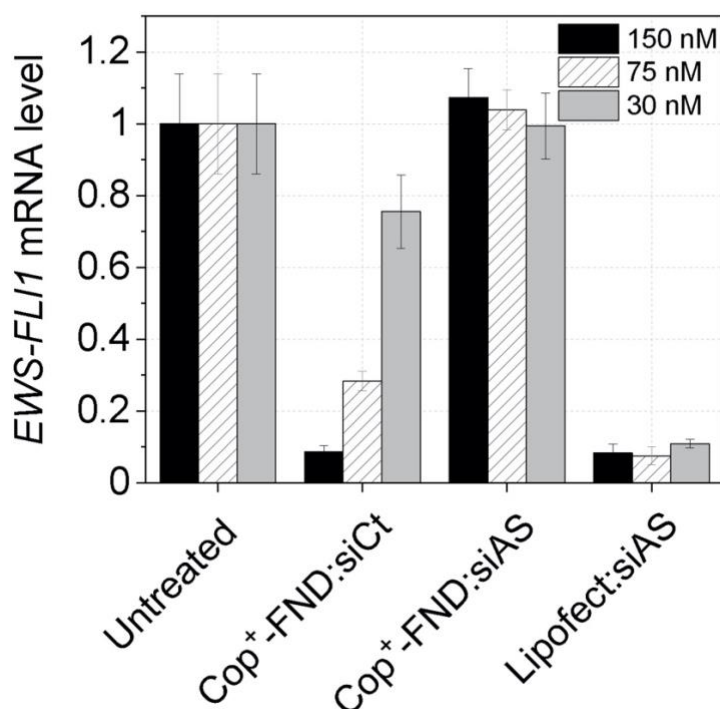


Figure S2. *EWS-FLI1* oncogene inhibition (measured by RT-qPCR) by Cop⁺-FND complexed with different concentration (30, 75, 150 nM) of siRNA AntiSense (siAS) directed against *EWS-FLI1* junction oncogene or Control (irrelevant siRNA, siCt), and compared to siAS complexed with Lipofectamine 2000 (Lipofect 2000, as a positive control, used without serum added to the medium), at different siRNA concentrations. Cop⁺-FND:siRNA mass ratio was kept constant and equal to 65:1. mRNA *EWS-FLI1* was extracted 24 h after incubation.

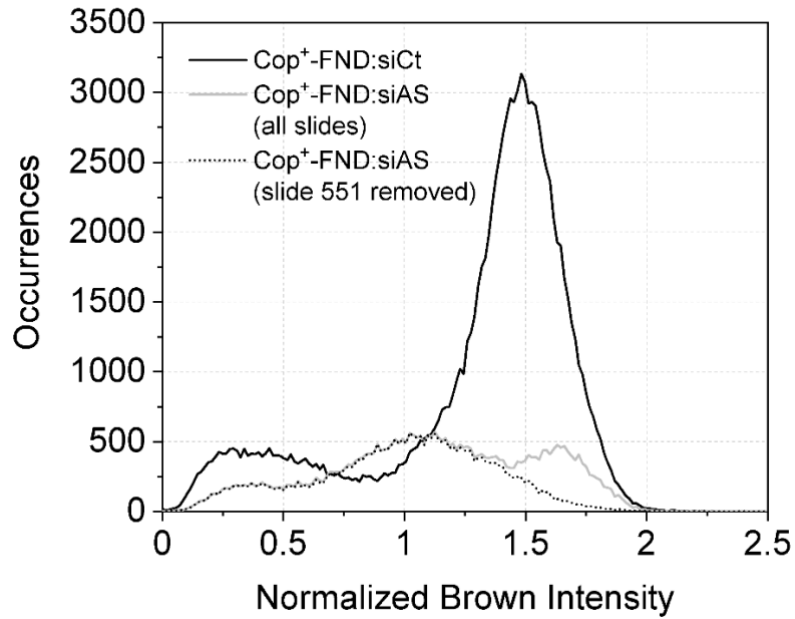


Figure S3. Distributions of EWS-FLI1 immunostaining intensity within individual cell nucleus of tumor region selected by the histopathologist. Two groups are displayed: animals treated by Cop⁺-FND:siCt (black solid line, data of 4 mice pooled) and Cop⁺-FND:siAS (grey solid line, data from 5 mice). In the case of Cop⁺-FND:siAS, the slide histological preparation #551 (1 mice) yielded a high staining intensity, larger than the one of Cop⁺-FND:Ct, which led us to suspect a labeling issue specific to this sample. After removing this problematic slide (black dashed line, 4 mice) we obtain similar shapes for Cop⁺-FND:siCt and Cop⁺-FND:siAS with two peaks, one at low intensity (around 0.3) corresponding to EWS-FLI1 negative labeling and the other one at high intensity (≈ 1.5 in the case of Cop⁺-FND:siCt) associated to positive nuclei. Cop⁺-FND to siRNA mass ratio of 25:1.
